Trottenberg *et al. EPJ Techniques and Instrumentation* (2018) 5:3
https://doi.org/10.1140/epjti/s40485-018-0044-2

EPJ Techniques and Instrumentation
a SpringerOpen Journal

RESEARCH Open Access

An interferometric force probe for beam diagnostics and the study of sputtering

Thomas Trottenberg*, Alexander Spethmann and Holger Kersten

*Correspondence:
trottenberg@physik.uni-kiel.de
Institute of Experimental and Applied Physics, University of Kiel, Leibnizstraße 19, D-24098 Kiel, Germany

Abstract

A novel probe for the measurement of forces exerted by a beam of ions and neutral atoms on a small target is described. The force probe is intended for various applications: First, diagnostics of thruster plumes of electric spacecraft propulsion engines, in particular the determination of the spatial distribution of the momentum in an exhaust beam, and second, the study of sputtering of solid targets by means of the related momentum transfer. The instrument makes use of a sensitive cantilever whose elastic deflection is measured interferometrically along two axes and enables that way a simultaneous measurement of two independent components of the force vector. The present contribution focuses on setup and calibration of the probe. Example measurements with obliquely irradiating ion beams are performed.

Keywords: Sputtering, Momentum transfer, Force measurement, Beam diagnostics, Electric spacecraft propulsion

Introduction

Diagnostics for exhaust plumes of electric spacecraft propulsion engines are often based on electric probes like Faraday cups [1] and retarding field analyzers [2]. Spectroscopic techniques like optical emission spectroscopy [3], laser absorption spectroscopy [4], and laser-induced fluorescence [5] are also applied, but less frequently. Recently, force measurements were performed in the beam of an industrial broad-beam ion source that is very similar to the plume of gridded ion thrusters [6]. The advantage of the force measuring method over the standard electric techniques is that the latter are sensitive only for the charged species. This is an important issue because thruster plumes often contain a non-negligible amount of energetic neutral atoms [7]. Energetic neutral atoms originate from charge-exchange collisions with the gas behind the exhaust, which unintentionally escapes from the thruster, and with residual gas in the test chamber [8, 9]. In this contribution, we describe in detail a novel technique for the measurement of forces exerted by a thruster plume on a small test surface.

Recently, force measurements have also been applied for the study of sputtering [10–12]. When sputtering occurs, not only momentum carried by the impinging beam particles is transferred to the irradiated surface, but momentum also leaves the surface together with, firstly, the sputtered target atoms and, secondly, re-emitted beam particles. The measured force is an average, just like the sputter yield is an average, but it contains different information. The force is a vectorial quantity, and the involved particles are differently weighted in the averaging integral according to their directions, speeds,

and masses. Therefore, force measurements provide information about sputtering beyond the scalar sputter yield, and comparisons of measured forces with computer simulations would be a stronger test for numerical models than comparisons of sputter yields.

Another field of application of force measuring techniques emerged recently in the context of plasma–wall interaction. The forces exerted by low-temperature low-pressure plasmas on the surface of solid boundaries are comparable to the forces that occur in the aforementioned thrust measurements and sputtering experiments [13, 14]. A method similar to the technique presented in this article was recently applied for a precise measurement of the "plasma pressure" by means of a force probe that was integrated into a plane plasma boundary [15].

In comparison with our formerly reported force measurements that used electromagnetically compensated pendula [6, 11, 16, 17], the here presented probe is based on a sensitive cantilever whose deflection is measured interferometrically along two axes.

Scanning a cross section of a thruster plume yields vectorial information about the momentum distribution in the plume. In comparison with a thrust balance, the thrust vector could be calculated from the measured force profiles: Integration over the entire cross section yields the thrust vector, and not only the scalar thrust component defined by the orientation of the thrust balance. On the other hand, the measured "differential thrust" at a specific point in the plume, i.e. the spatially resolved momentum flux density, is valuable information for improvements of the efficiency of a thruster.

A further application of force probes is the experimental study of momentum transfer from energetic ions and atoms to solid targets, at which sputtering not necessarily occurs. For example, air molecules interact with surfaces of space vehicles, especially of satellites and small objects in low Earth orbits. A force probe with targets of different materials mounted on a satellite could provide a direct measurement of material specific drag data when the angle of approach of the target surface is varied. From such empirical data, drag coefficients of satellites could be calculated with high accuracy [18].

The article is arranged as follows. A detailed description of the force probe is given in the "Description of the probe" section. The following "Calibration and errors" section is dedicated to the calibration of the probe and the accuracy and temperature stability of the method. The "Example of a vectorial force measurement" section presents, as an example, a force vector measurement in that an ion beam impinges at variable angles of incidence at the target. Finally, an Appendix contains, as a supplement to the "Calibration and errors" section, a theoretical treatment of the eigenmodes of the probe that is useful for the understanding of the mechanical noise.

Description of the probe

The force probe uses for sensing a thin cantilever, which is an often applied technique in many fields [19]. A small circular target with a diameter of 20 mm is mounted at the free end of the Al_2O_3 ceramic tube that serves as the 172 mm long cantilever (see Fig. 1). The target will be exposed to a particle beam, for example in a vacuum chamber for testing of electric space propulsion systems, while the cantilever itself is protected from the particles. When a force acts on the target, the tube is elastically bent (not more than a few micrometers), so that each point of the cantilever is minimally displaced from its initial position. In terms of the theory of elasticity, the cantilever is essentially a hollow cylindrical beam with one fixed end. The displacement of a specific part of the

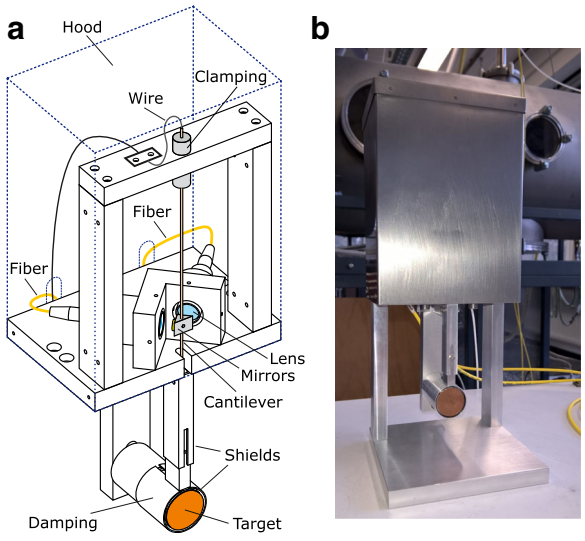

Fig. 1 Implementation of the force probe. **a** Drawing with the inner parts of the probe, **b** photograph of the probe before mounting in the vacuum chamber (in the background). Note the circular copper target and the two yellow fiber optic cables

cantilever serves as the quantity to be measured; the movements occur mainly in the plane perpendicular to the cantilever.

The tube geometry, i.e. a hollow cylinder, was chosen with regard to the elastic properties that are in this case the same for all bending directions; moreover, this geometry allows to feed a wire through the cantilever. Such a wire is connected to the aluminum target holder and can be used for biasing and measurements of the current taken by the conductive target.

In order to determine the two-dimensional deflection, two orthogonally oriented interferometric displacement sensors are used, which measure the displacements of two small mirrors attached to the cantilever. The circular mirrors with diameters of 5 mm are bonded to the perpendicular faces of a triangular prism, and the polyvinyl chloride prism with a bore through its base faces is plugged on the ceramic cantilever tube as shown in Figs. 1 and 2.

The interferometric displacement sensor is a commercial product (attoFPS 3010) from the Attocube Systems AG, Germany [20, 21], which applies the frequency-modulation continuous wave (FMCW) interferometer method [22]. It uses the path between a plane end of a single-mode fiber and a mirror as cavity, where a lens (focal length 8.18 mm, diameter 9 mm) is placed between fiber and mirror. The lens in the sensor head has a distance of its focal length from the fiber end in the connector (known as FC/PC connector), so that the light from the fiber leaves the sensor head as a thin beam of parallel (collimated) rays with a diameter less than 2 mm. The mirrors have a distance of approximately 6 mm from the respective lenses.

Approximatly 4% [20] of the 1550 nm laser light (150 μW) from a tunable distributed feedback (DFB) laser are reflected backwards at the plane end of the fiber and serve as the reference wave, while most of the light leaves the fiber and reaches the mirror. The light reflected at the mirror could directly re-enter the fiber through the same plane end and finally interfere with the reference wave at the detector outside the vacuum chamber at the

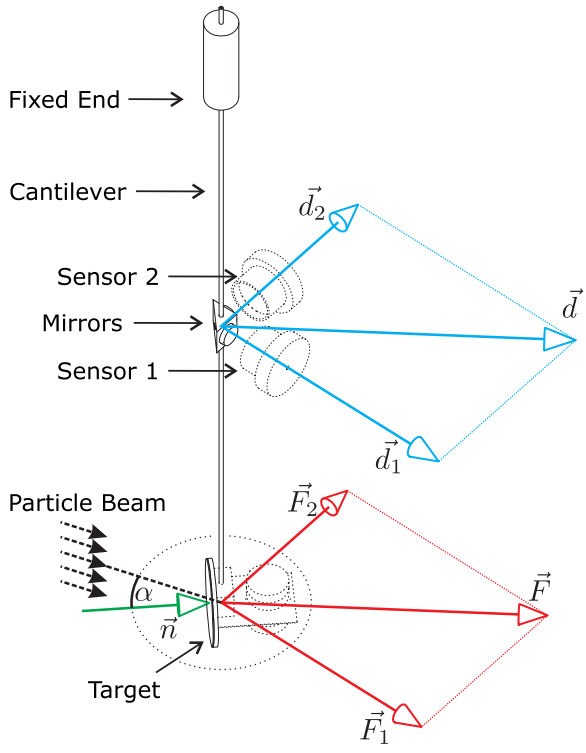

Fig. 2 The drawing of the essential parts shows that a force $\vec{F}$ acting at the target is related to a displacement $\vec{d}$ of the mirrors. The indexed components $\vec{d}_1$ and $\vec{d}_2$ of the displacement are measured through the two sensor optics and correspond to the two indexed force components $\vec{F}_1$ and $\vec{F}_2$. The forces, the target normal $\vec{n}$, and the incidence angle α of the beam belong to the same plane sketched by a dotted circle

other end of the wave guide. However, this single-path technique has two disadvantages: first, the mirror has to be aligned very precisely in order to receive and reflect the light rays perpendicularly, and second, the wave coming from the mirror has a much higher intensity than the reference wave. In such a case, the difference between constructive and destructive interference is only weekly pronounced (low signal contrast) and might not be detectable. For this reason, the wave from the mirror is attenuated by the following 'trick': The mirror is slightly misaligned by a small rotation ($< 1°$) of the cantilever about its axis, so that the returning light is not focused on the fiber core, but rather with a small lateral shift at the zirconia ferrule of the connector. (This can be done by turning the stainless steel cylinder with fine thread at the fixed end of the cantilever, when a locking screw is loosened.) That way, strayed and significantly attenuated light is reflected and collimated by the lens, passes the cavity once again in both directions, and is focused this time right at the fiber core, where it finally re-enters. This patented 'self-aligning' dual-path technique was described and investigated in detail by Thurner, Braun, and Karrai [20].

In order to overcome the typical drawbacks of a conventional Fabry-Pérot interferometer, i.e. low sensitivity sensing spots at the interference extrema and the ambiguity of the displacement direction, the interferometer modulates the laser wavelength (about $\pm 10^{-3}$ wavelengths) periodically with a frequency of 12.5 MHz. This fast tuning is accomplished in the DFB laser by means of a modulation of the current that powers the laser diode [21–23]. The use of optical fibers and vacuum feedthroughs allows to keep the cavity

length short and to have only non-electric parts in the probe itself, while the electronic parts are placed outside the vacuum chambers in which the probe is applied.

Now, we come back to our mechanical setup. The masses of the mirror unit, the target with its holder, and the ceramic tube give rise to undesired mechanical vibrations. In particular, the pumps of vacuum chambers always excite eigenmodes; but also an abrupt change of the force that is to be measured would cause a ballistic overshoot beyond the equilibrium position and subsequent weakly damped oscillations.

Figure 3 shows a modal analysis of measured displacements of the mirrors. The sampling rate of the displacement sensors, 1.5 kHz, is well above the frequencies of the expected mechanical modes. The probe is placed for this test measurement on a laboratory table without special damping provisions. The x-y plot in Fig. 3a displays two seconds (green curve) of the two time series of orthogonal displacements. The oscillations along the first and second axis extend up to $\pm 0.8\,\mu$m and $\pm 1.2\,\mu$m, respectively. In general, the amplitudes are changing on a time scale of seconds. We attribute this to irregular exitation amplitudes from the environment and an unavoidable coupling between several modes of the entire setup.

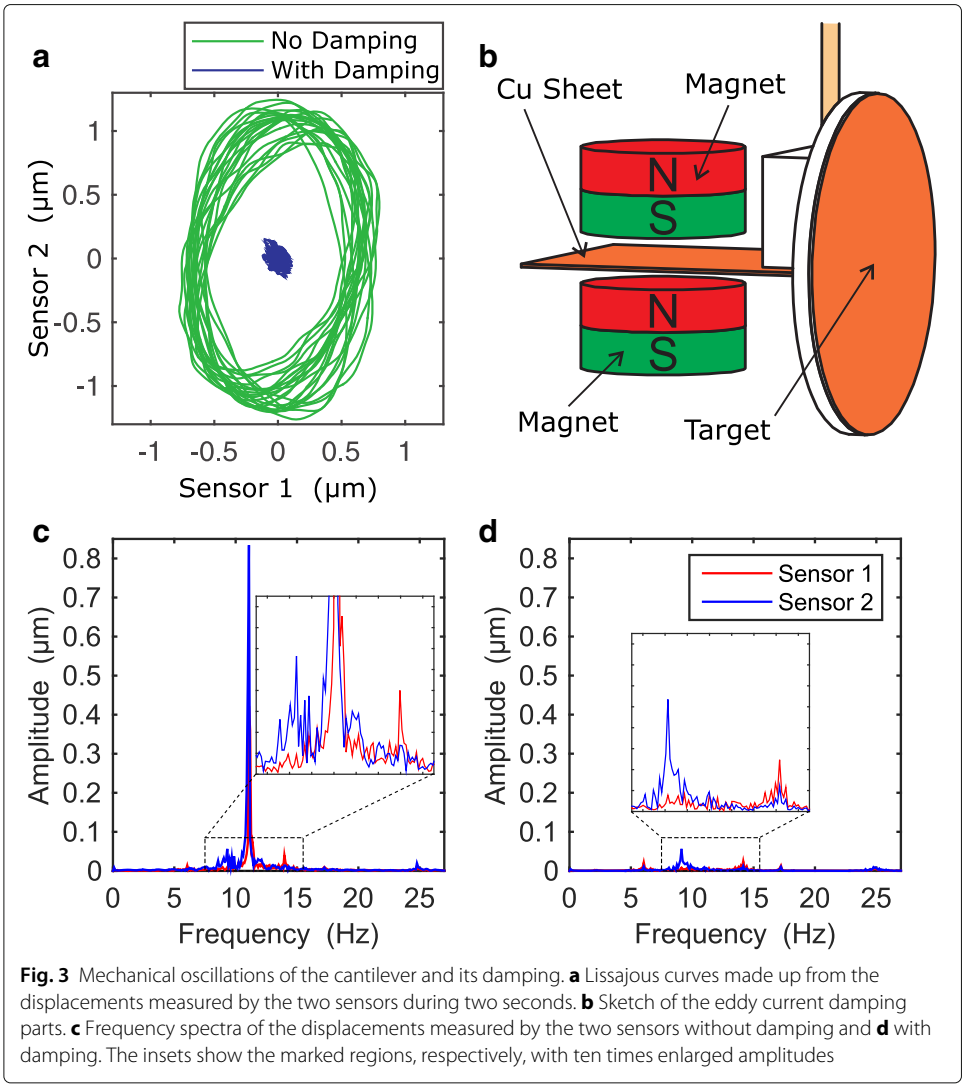

Fig. 3 Mechanical oscillations of the cantilever and its damping. **a** Lissajous curves made up from the displacements measured by the two sensors during two seconds. **b** Sketch of the eddy current damping parts. **c** Frequency spectra of the displacements measured by the two sensors without damping and **d** with damping. The insets show the marked regions, respectively, with ten times enlarged amplitudes

The frequency analysis (twice the absolute values of the single-sided discrete Fourier transforms divided by the number of samples) of the 10 s long time series of the displacements in Fig. 3c exhibits one distinct peak at $f_0 = (11.1 \pm 0.1)$ Hz, and no significant amplitudes are found beyond 25 Hz.

A simplified theoretical model can be used with the purpose of identifying the observed mode. Our model is an application of the Euler-Bernoulli beam theory for a homogeneous thin beam with two point masses, which is described in the Appendix of this article. The two point masses $m_1 = 3.85 \times 10^{-4}$ kg and $m_2 = 1.78 \times 10^{-3}$ kg (calculated from the dimensions of the parts) are at the positions $x_1 = 78$ mm and $x_2 = 172$ mm measured from the fixed end, and the linear mass density of the vibrating ceramic beam is $m = 2.25 \times 10^{-3}$ kg m^{-1} (for the density of 3825 kg m^{-3} given by the manufacturer). Furthermore, we assume the modulus of elasticity $E = 3.09 \times 10^{11}$ Pa for the Al_2O_3 ceramic at room temperature [24] and use $I = \frac{\pi}{4}\left(r_1^4 - r_2^4\right)$ as the second moment of area of the cantilever cross-section for the direction of the bending. Note that I is independent of the bending direction because of the rotational symmetry of the cross section. The model results in a first mode at a frequency of $f_1 = 10.6$ Hz, and subsequent eigenmodes at $f_2 = 124.7$ Hz, $f_3 = 588.6$ Hz, and $f_4 = 1269$ Hz. Figure 4 shows the corresponding modes. The $n = 1$ mode is an in-phase oscillation, at which the mirror unit and the target unit move always in the same direction. The $n = 2$ mode corresponds to an anti-phase oscillation of the mirrors and the target. However, the modes $n > 1$ cannot be found in the measured spectra. The good approximation of the calculated f_1 frequency with the measured natural frequency f_0 identifies this one as a mode 1 vibration.

The vibrations at the natural frequency f_0 do not constitute a serious drawback for force measurements as long as the displacements caused by the force are not too small in comparison with the mechanical noise. Averaging over several periods of the natural frequency reduces the noise.

However, in order to keep the required sampling time for the averaging short, the probe is equipped with a damping mechanism. Figure 3b shows the essential parts of the eddy current damping unit. A pair of small cylindrical permanent magnets provides a magnetic field that penetrates a thin copper sheet attached to the back side of the target

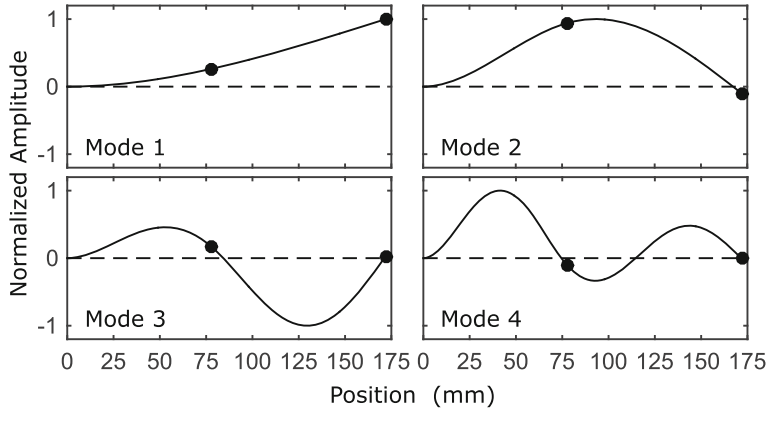

Fig. 4 Calculated shape functions of the first four eigenmodes of the cantilever. The amplitudes are normalized to the maximum local amplitude, respectively. The markers indicate the positions x_1 and x_2 of the two point masses M_1 and M_2, which represent the mirror and the target units

holder. The target together with the copper sheet oscillates perpendicularly to the field lines, so that eddy currents are generated in the sheet. The currents create a counteracting force (Lenz's law) and dissipate energy stemming from the oscillation. Figure 3a shows the x-y plot of the measured displacements for the damped case (blue curve), too. Now, the oscillations are significantly reduced in both directions. The natural frequency f_0 disappeared completely from the spectra shown in Fig. 3d, which indicates the efficient damping of the cantilever vibrations. In contrast, the amplitudes at other frequencies persist; the remaining frequencies can be understood as the complicated modes of the entire setup that result not only in vibrations of the lenses but also of the damping unit, which are unintentionally transmitted to the target via the eddy currents. We determined the time constants τ for the exponentially decaying amplitudes, i.e. decaying proportionally to $\exp(-t/\tau)$ with the time t. To this end, we knocked carefully on the target with a thin wire and recorded the oscillations. We found $\tau = (6.0 \pm 0.5)$ s without eddy current damping, and $\tau' = (0.3 \pm 0.1)$ s with the damping unit. The resulting quality factor $Q = \frac{1}{2}\omega_0\tau$ for the cantilever as an oscillating system becomes $Q = 209 \pm 18$ without additional damping and $Q' = 10.5 \pm 3.5$ for the intentionally damped system. This means that the damped cantilever looses its oscillation energy after only a few ($\approx Q'/2\pi$) oscillations, but it is still underdamped ($Q' > 1/2$), i.e. abrupt displacements cause an overshooting. In the "Example of a vectorial force measurement" section, a measurement without damping will be shown in comparison with a corresponding measurement with the damping system.

The method requires a reference measurement without the force that is to be determined. The reference measurements are performed shortly before or after the main measurement with the force. This method ensures that temporal mechanical changes of the experimental setup are not misinterpreted as forces. For example, in electric propulsion test chambers, diagnostics are usually mounted on mechanical structures that are exposed to the truster plume. The structures are unintentionally heated and give rise to small displacements. Thus, the gravity vector could slightly be tilted relative to the probe, so that the cantilever with the masses of the target and mirror assemblies adopts a different equilibrium position with changed displacements d_1 and d_2. Such drifts occur at time scales much longer than a measurement, which can be performed within a few seconds, and become negligible when reference measurements are performed shortly before or after the main measurement. A practical procedure will be described in the "Example of a vectorial force measurement" section.

Calibration and errors

For calibration, the instrument is laid on its rear side so that certified weights of 1, 2, 5, and 10 mg (± 0.006 mg) can be put on the target surface. Combinations of up to four of the weights with the total mass m exert the force $F = mg$ on the target, where $g = 9.81\ \mathrm{ms}^{-2}$ is the local gravitational acceleration. For the calibration, the damping unit is removed, because the cantilever is bent almost 3 mm due to the weight of the mirrors and the target holder; the target holder would rest on the damping unit.

The weights are put on the center of the target, which is possible within a radius of 3 mm. In our case, no special measures are taken for an exact horizontal orientation, since even a slope angle of the cantilever of 5 degrees would cause a reduction of the measured

component of less than 0.4 % (cosine of the angle). Furthermore, a rotation about the cantilever axis would cause asymmetric displacements measured by the two sensors, which not affects the magnitude of the measured force (vector sum of the two components).

Figure 5 displays the two orthogonal components of the displacements measured by the two sensors and the absolute value of their vectorial sum versus the force exerted by the weights. We obtain a calibration constant of $k = 23.4\,\mathrm{N\,m^{-1}}$.

The error of k, i.e. the uncertainty of the slope of the regression line, is, due to the number of data points, smaller than the least significant specified digit and therefore negligible. However, the standard deviation of the individual measurements from the regression line is 0.09 μm, corresponding to 2.1 μN.

The following calculation can be used to estimate the order of magnitude of the calibration constant. The underlying theory of the deformation of solids can be found in many textbooks, e.g. [25]. The geometrical and material parameters of the cantilever are the same as in the "Description of the probe" section.

The stiffness $S = F/\delta$ describes the deflection δ of the free end under the action of the force F at the free end as a special case of Hook's law. The stiffness of the cantilever beam

$$S = \frac{3EI}{x_2^3} \tag{1}$$

can be calculated from Young's modulus E and the second moment of area I of the cantilever cross-section, which both were already used in the "Description of the probe" section. Note that not the deflection at the free end, where the target is mounted, is measured but the deflection d at the position x_1 of the mirrors. The deflection at this specific position on the beam can also be calculated [25], and the deflection-to-force conversion factor $k = F/d$ becomes

$$k = \frac{F}{d} = \frac{6EI}{x_1^2(3x_2 - x_1)} \quad . \tag{2}$$

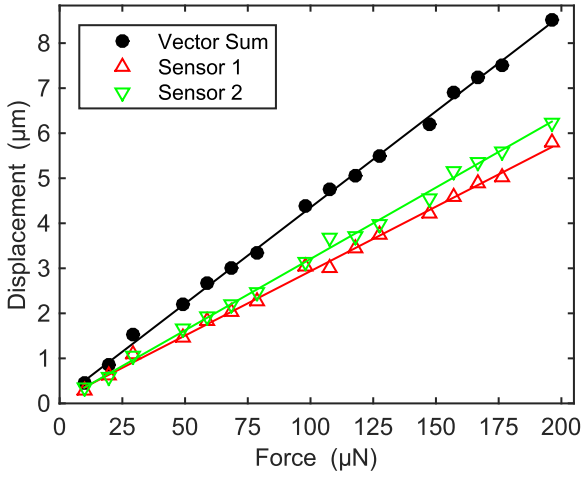

Fig. 5 Calibration measurement. The abscissa represents the force exerted by certified weights. The displacements d_1 and d_2 of the two sensor axes are plotted as well as the magnitude of their calculated vector sums $d = \left|\vec{d}_1 + \vec{d}_2\right|$. The slope of the regression line for the vector sums yields the calibration constant $k = 23.4\,\mathrm{N\,m^{-1}}$. Note the different slopes of the lines for two sensors, which result from a small rotation of the calibration setup about the cantilever axis; this small misalignment has no effect on the vector sum, the (calculated) misalignment angle is approximately 3°

Assuming again an elastic modulus $E = 3.09 \times 10^{11}$ Pa for the Al_2O_3 ceramic at room temperature [24], one would expect $k = 32.8\,\mathrm{N\,m^{-1}}$. This is the correct order of magnitude, but the measured value is almost 30% smaller. One part of the difference can be attributed to the tolerance in the radii (±5%) on which k strongly depends. Furthermore, the elasticity of the polycrystalline material is only imprecisely known, since the elastic modulus E depends on purity, size of the crystallites, and the porosity, which all result from the manufacturing method.

Finally, we discuss the influence of the cantilever temperature T on the deflection-to-force conversion factor. Young's modulus $E(T)$ of the alumina specimen investigated in the above mentioned study [24] decreased linearly with increasing temperatures $T < 900\,^{\circ}\mathrm{C}$, and a plot in that publication shows a negative slope of approximately $\mathrm{d}E/\mathrm{d}T = -4 \times 10^7\,\mathrm{Pa\,K^{-1}}$. A temperature rise of $\Delta T = +100\,\mathrm{K}$ starting from room temperature (293 K) lowers the elastic modulus E by 1.3% ($E = 3.05 \times 10^{11}$ Pa), and the calibration constant k decreases consequently by 1.3%, too. When a significant warming of the cantilever is expected, this effect should be considered.

There is a simple way how a changing "spring constant" k could be monitored without additional temperature sensors, which obviously should not be attached to the cantilever. However, this technique works only when the damping unit is not used, because it relies on an evaluation of small shifts of the natural frequency f_0. For an ideal beam with one free end and no additional masses attached to it, the square of the natural frequency f_0 is proportional to Young's modulus E, i.e. $f_0^2 \propto E$. One can easily reason that this holds for the geometrically more complicated force probe cantilever as well, since the elastic modulus E still enters linearly in all the forces that move the cantilever. Hence, an increase of E by a factor of λ makes the motion by the factor λ^2 faster (time scales proportionally to λ^{-2}), i.e. frequencies of oscillations would increase by the factor λ^2. This is confirmed by the above mentioned theoretical modal analysis in the Appendix, in particlular Eq. (8), which results in a decrease from 10.6 Hz to 10.5 Hz for the first mode, when the temperature rises by $\Delta T = +100\,\mathrm{K}$ from room temperature. A by 1% ($\lambda = 0.99$) lower frequency f_0 would indicate a by 2% ($\lambda^2 = 0.98$) smaller conversion factor k. A frequency drift of such an amount is detectable, see Fig. 3.

Example of a vectorial force measurement

In this section, an experiment is performed in order to demonstrate the capability of the probe to measure forces as vectors. For this purpose, the force is generated in a vacuum chamber by a mixed Ar/Ar^+ beam that impinges at variable angles of incidence α at the probe target, see Fig. 6a [12].

The force probe is mounted on a turnable platform driven by a step motor with an angular resolution of $\Delta\alpha = 1.8^{\circ}$. The cantilever coincides with the vertical rotational axis of the turnable platform, so that the target remains at the symmetry axis of the ion beam when the probe is rotated. The beam is provided by a broad-beam ion source with grid system [17, 26]. The distance from the beam source to the target is 88 cm. At this distance from the grid system of the broad-beam ion source (diameter 125 mm), inhomogeneities of the beam can be neglected (compare [11], where the target was bigger and the distance from the source was shorter).

The plasma in the ceramic source chamber, from where the ions are extracted, is generated by a 2.45 GHz electron cyclotron resonance microwave discharge at an Ar gas flow of

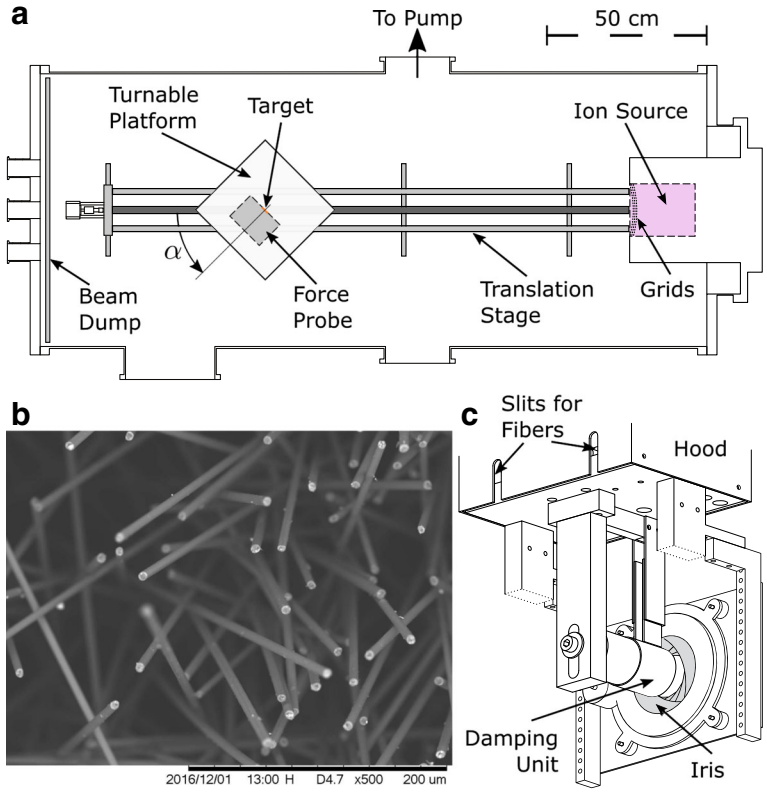

Fig. 6 Application of the force probe. **a** Top view of the vacuum chamber used for the example measurements. The tilt angle α indicates the rotation of the platform with the force probe. This angle is the angle of incidence of the ions emitted from the ion source that impact at the force probe target. **b** Scanning electron microscopy image of the carbon fiber velvet. **c** Force probe with beam shutter. The drawing shows the setup with the blade iris half open (gray shaded) from behind. (This optional device is not used in the example measurements)

5 sccm. The potential of the source plasma is anchored by means of an anode at a potential of $U_a = +1200\,\mathrm{V}$ in order to accelerate the extracted ions in the grid system, which separates the source chamber plasma at the high potential from the target chamber plasma at a low potential. The kinetic energy of the accelerated ions in the target chamber is therefore approximately $E_{kin} = 1.2\,\mathrm{keV}$. A more detailed discussion of the kinetic energies in the beam can be found in [9].

The vacuum chamber is a stainless steel cylinder with an inner diameter of 65 cm and a length of 160 cm, see Fig. 6a. The argon gas pressure in the target chamber is 2×10^{-2} Pa achieved by a turbo molecular pump (pumping speed $500\,\mathrm{l\,s^{-1}}$) in combination with a rotary vane pump ($60\,\mathrm{m^3\,h^{-1}}$).

Each force measurement consists of a previous reference measurement when the beam is off and a subsequent main measurement during beam operation. Thereafter, the beam is switched off, and the displacement is measured again. The time series of such a measurement procedure for the two axes are displayed in Figs. 7a and b. The deflections of the two axes are unequal in Fig. 7a because of the oblique angle of incidence, which is $\alpha = 45°$ in this case.

For the determination of the displacements in the three periods of time, the respective averages are calculated (the data closer than 0.2 s to the switching time

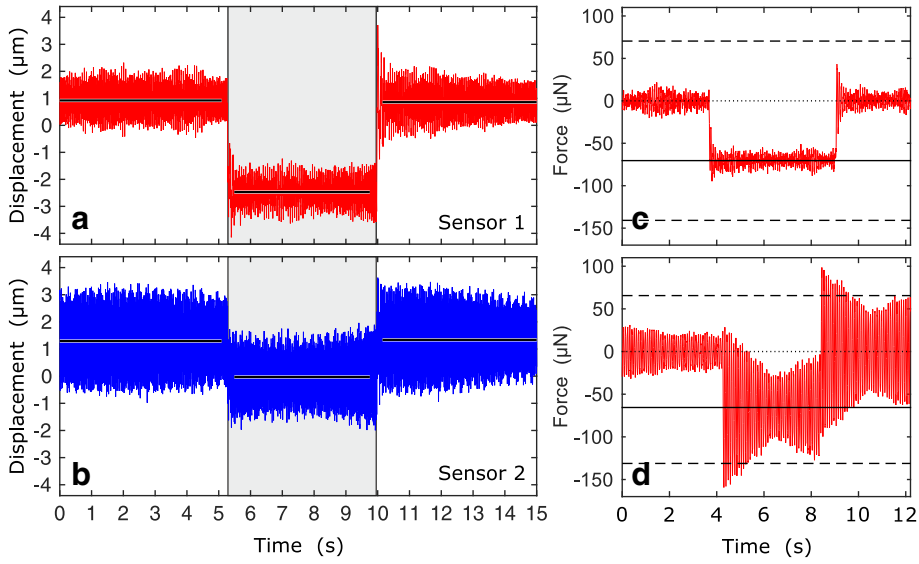

Fig. 7 Time series of the displacements measured along the two sensor axes with a copper target, **a** and **b**. The shaded time spans indicate when the ion beam is switched on and exerts a force on the probe target. The horizontal lines are averages for the respective time spans. The angle of incidence is 45°. The difference between a measurement with and without the eddy current damping system is shown in (**c**) and (**d**), respectively. In this case, the angle of incidence is 0° (perpendicular incidence), and only the signals from sensor 1 are displayed. Note the overshooting in case of the undamped probe. The kinetic energy of the argon beam particles is 1.2 keV in all measurements

points are excluded from the averaging). The average displacements are indicated in Figs. 7a and b by horizontal lines. The difference between the two averaged reference displacements is related to the repeatability of the individual measurement and is displayed as error bars in Fig. 8.

Figure 7c and d demonstrate the effect of the eddy current damping. In case of the removed damping system, an overshooting and subsequent persistant oscillations occur at every switching. The amplitude of the overshooting and the oscillations is comparable to the causal signal itself, i.e. the signal-to-noise ratio is here about unity.

In case of the time series shown in Fig. 7, the probe target is a copper foil, so that sputtering and a release of momentum together with the outgoing particles (repulsion) is to be expected. Consequently, the measured force is larger than the force that a perfectly absorbing and not sputtering material experiences. Carbon has a low sputtering yield and is therefore often used for beam dumps in test chambers. Moreover, the effective sputter yields can be reduced even more by means of an appropriate topography of the surface. Carbon fiber velvet (produced by the Energy Science Laboratories, Inc.) is such a material; it consists of approximately 2.2 mm long and 7 μm thin carbon fibers that arise perpendicularly from a plane base. Figure 6b shows a scanning electron microscopy image of the fibers. The geometry, which resembles a brush with extremely thin bristles, allows the ions to enter deeply into the carbon fiber velvet. Consequently, sputtered carbon from one fiber is re-deposited at other fibers with high probability, and reflected ions likely undergo more than one contact with the fibers before they leave the material.

Now, measurements at variable angles of incidence α are performed with the copper foil and the carbon fiber velvet. Figure 8a shows the measured displacements $d_1(\alpha)$ and

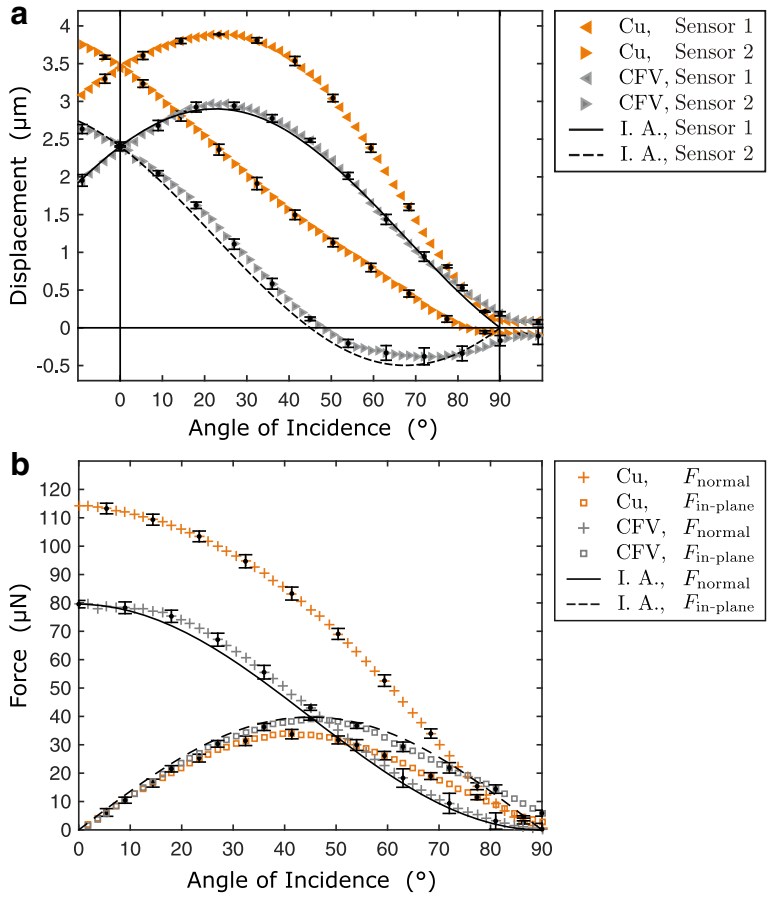

Fig. 8 Measurements at different angles of incidence. **a** Diplacements measured by the two sensors, **b** calculated normal and in-plane force coordinates of the same data. The forces are caused by a 1.2 keV Ar/Ar$^+$ beam impacting on a copper (Cu) and a carbon fiber velvet target (CFV). The calculated solid and dashed lines indicate the theoretical case of ideal absorption (I.A.) without sputtering. For the sake of legibility, only every fifth error bar is plottet

$d_2(\alpha)$ for the angles $\alpha = -10° \cdots + 100°$, while Fig. 8b displays the forces $F_1 = k\,d_1$ and $F_2 = k\,d_2$ transformed into a more practical coordinate system: One component, F_{normal}, points along the inward directed target normal, and the other one, $F_{\text{in-plane}}$, is the projection of the force vector onto the target surface. The transformations of the components are

$$F_{\text{normal}} = \sqrt{\frac{1}{2}}\,(F_1 + F_2)$$
$$\text{and} \qquad F_{\text{in-plane}} = \sqrt{\frac{1}{2}}\,(F_1 - F_2). \tag{3}$$

Note the equality of the displacements, $d_1 = d_2$, for the angle $\alpha = 0°$, and that the axes change roles when α changes its sign due to the symmetric setup (Fig. 8). For increasing oblique incidence angles $\alpha > 10°$, the flux onto the target becomes more and more reduced, and one could expect that the flux vanishes for extremely grazing incidence, $\alpha \approx 90°$. However, due to the finite diameter of the ion source and the beam divergence, some beam particles strike the probe target even at $\alpha > 90°$. This explains the not vanishing deflections for $\alpha \geq 90°$.

Before we discuss the difference between the two targets, we come back to the hypothetical case of a perfectly absorbing and not sputtering material. In this case, the beam particles transfer their entire momentum to the target, and no further momentum exchange occurs. The angle-of-incidence dependent two force components F_1 and F_2 can be described by the functions

$$\begin{aligned} F_1(\alpha) &= F_0 \cos\alpha \cos(\alpha - 45^\circ) \\ \text{and} \qquad F_2(\alpha) &= F_0 \cos\alpha \cos(\alpha + 45^\circ), \end{aligned} \tag{4}$$

where F_0 is the magnitude of the force vector at perpendicular incidence, i.e. $F_0 = \sqrt{F_1^2(0^\circ) + F_2^2(0^\circ)}$. The Eqs. (4) account by their $\cos\alpha$ terms for the reduced flux at oblique incidence and express by the second cosines the projection of the force vector onto the respective directions of the displacement sensors. These theoretical functions are plotted (as the corresponding displacements) in Fig. 8a, where the amplitude F_0 was taken from the measurement with the carbon fiber velvet at perpendicular incidence ($\alpha = 0^\circ$).

The measurements with the carbon fiber velvet roughly follow the model of pure beam absorption, the small deviations can be summarized in two observations: First, both force components vanish at $\alpha = 90^\circ$ according to the discussion above; and second, the measured force components tend to be slightly more positive than the theoretical ones. The latter can be attributed to an imperfectly inhibited sputtering that still causes additional repulsion directed at some angle into the target.

In case of the copper target, the deviations from the pure absorption case are much more pronounced. Most obviously, the forces (displacements) at perpendicular incidence ($\alpha = 0^\circ$) are significantly, by 44%, enhanced. Moreover, the force measured by the second sensor does not vanish at $\alpha = 45^\circ$, it rather has a magnitude of approximately 0.4 of the F_2 value at $\alpha = 0^\circ$. At this oblique angle of incidence, the second sensor is directed perpendicularly to the beam direction, so that the measured force can only be caused by particles that leave the target with momentum.

Finally, we introduce an optional component that becomes necessary for measurements in environments where it is not feasible to repeatedly switch the beam on and off for the reference measurements. For this purpose, a beam shutter can be placed directly in front of the probe target. The shutter shown in Fig. 6c consists basically of a blade iris that has a maximum aperture of 36 mm and can be closed completely. A small direct-current motor drives the blades for quick opening and closing. Measurements in the plume of a Hall thruster have recently been performed and are planned to be published soon.

Conclusion

This article presented an instrument for the measurement of vectorial forces that are exerted on a small target exposed to a particle beam. The functional principle is based on an elastically bendable cantilever with one fixed end and the target mounted at the free end. The deflection of the cantilever is measured with an interferometric displacement sensor. Between the free and the fixed ends, two mirrors are attached that reflect the laser light from the sensor optics. By means of this arrangement, the displacement can be recorded in two dimensions, i.e. in the plane perpendicular to the cantilever beam.

Typical deflections are in the order of magnitude of a few micrometers, corresponding to some tens of micronewtons. The Fabry-Pérot type interferometer setup uses fiber optics, one for each of the two axes, which allow that only the small cavity parts have to be integrated in the probe, while the laser and the data acquisition electronics are operated outside the vacuum chamber.

The calibration was performed by putting small weights directly on the target surface. For this purpose, the cantilever and the target were oriented horizontally, so that the weights acted roughly in direction of the surface normal.

An example of a force vector measurement was presented, where the energetic particles of a broad-beam ion source impacted at variable angles at the probe target. Two different target materials were used, namely copper and a microstructured carbon fiber material with low volume filling factor (carbon fiber velvet). The forces measured with the carbon material showed an angle-of-incidence dependence expected from a perfect particle absorber without sputtering. In case of the copper target, the measured forces were not only enhanced in comparison with the carbon fiber material, but also the angle dependence changed. In particular, at an angle of 45°, the force components perpendicular to the beam direction differed qualitatively from each other: While this component practically vanished in case of the carbon fiber material, almost 40% of the value for perpendicular incidence was measured with the copper target. This was clear evidence for the repulsion caused by sputtered target atoms and re-emitted argon beam particles.

The force probe is therefore a promising diagnostic for the study of sputtering. When equipped with target materials like the carbon fiber velvet, which are characterized by very low effective sputter yields, the measured forces equal the momentum flux of the absorbed beam without any modification by the momenta of released particles. A force probe with such materials is thus ideally suited for thruster development and testing in the field of electric spacecraft propulsion.

Appendix

The cantilever with the mirror and the target units as a vibrating system can be treated by means of the Euler-Bernoulli beam theory, e.g. [25], which is demonstrated in this Appendix.

The cantilever is approximated by a thin beam along the spatial coordinate x, while the small deflections $y(x,t)$ at the time t are perpendicular to the beam axis. The mirror and the target are represented by two point masses m_1 and m_2 at the positions x_1 and x_2. At the positions x between the fixed end and the first point mass and between the two masses, i.e. $0 \le x \le x_1$ and $x_1 \le x \le x_2$, the Euler-Bernoulli beam equation

$$\ddot{y}(x,t)m + y''''(x,t)EI = 0 \tag{5}$$

describes the shape of the beam, where EI is the flexural rigidity for the bending direction, and m is the mass per length unit of the beam.

From the Euler-Bernoulli beam theory, it is known that the possible (real) shape functions can be decomposed into the series

$$y(x,t) = \sum_{n=1}^{\infty} w_n(x)\cos(\omega_n t + \varphi_n) \tag{6}$$

of the modes n with the corresponding eigenfrequencies ω_n, where the individual modes are separated into a spatial amplitude function $w_n(x)$ and the oscillation in time with an arbitrary phase constant φ_n.

The well-known ansatz for the amplitude functions of a simple homogeneous beam with no additional masses is a linear combination of sine, cosine, hyperbolic sine, and hyperbolic cosine functions. The ansatz for a mode in our case, however, is piecewise defined by $y(x) = y_1(x)$ for $0 \le x \le x_1$ and $y(x) = y_2(x)$ for $x_1 < x \le x_2$; the parts are

$$\begin{aligned} y_1(x) &= a_1 \sin(\kappa x) + a_2 \cos(\kappa x) + a_3 \sinh(\kappa x) + a_4 \cosh(\kappa x) \\ \text{and } y_2(x) &= a_5 \sin(\kappa (x - x_1)) + a_6 \cos(\kappa (x - x_1)) \\ &\quad + a_7 \sinh(\kappa (x - x_1)) + a_8 \cosh(\kappa (x - x_1)) \end{aligned} \tag{7}$$

with the abbreviation

$$\kappa^4 = \frac{m}{EI}\,\omega^2. \tag{8}$$

The boundary conditions are as follows. The fixed end at $x = 0$ means

$$y_1(0) = 0 \quad \text{and} \quad y_1'(0) = 0. \tag{9}$$

The smooth transition at $x = x_1$ is expressed by

$$y_1(x_1) = y_2(x_1), \quad y_1'(x_1) = y_2'(x_1) \quad \text{and} \quad y_1''(x_1) = y_2''(x_1). \tag{10}$$

The second derivatives in the third equation have the meaning of the bending moment (when multiplied with EI), which is continuous for all x on the beam. In particular, the bending moment vanishes at the free end,

$$y_2''(x_2) = 0. \tag{11}$$

Finally, we have the equations of motion for the two point masses M_1 and M_2,

$$\begin{aligned} M_1 \ddot{y}_1(x_1) &= EIy_1'''(x_1) - EIy_2'''(x_1) \\ \text{and } M_2 \ddot{y}_2(x_2) &= EIy_2'''(x_2). \end{aligned} \tag{12}$$

The mass M_1 is moved by the shear forces EIy''' from both sides, whereas M_2 feels a force only from one side. Note, that the shear force along the beam has a discontinuity at $x = x_1$ due to the force M_1 exerts at that point. The equation of motion for a line element dx of the beam is already expressed by the Euler-Bernoulli beam equation Eq. (5).

The set of eight Eqs. (9) to (12) is linear in the coefficients $a_1, \ldots a_8$ for a specific κ. Therefore, it can be written with the ansatz for $w_n(x)$ from Eqs. (7) and its three derivatives as a matrix equation

$$\mathbf{M}(\kappa) \begin{pmatrix} a_1 \\ a_2 \\ \vdots \\ a_8 \end{pmatrix} = 0. \tag{13}$$

The Matrix reads

$$\mathbf{M}(\kappa) = \begin{pmatrix} 0 & 1 & 0 & 1 \\ \kappa & 0 & \kappa & 0 \\ c_1(\kappa) & c_2(\kappa) & c_3(\kappa) & c_4(\kappa) \\ \kappa\, c_2(\kappa) & -\kappa\, c_1(\kappa) & \kappa\, c_4(\kappa) & \kappa\, c_3(\kappa) \\ -\kappa^2\, c_1(\kappa) & -\kappa^2\, c_2(\kappa) & \kappa^2\, c_3(\kappa) & \kappa^2\, c_4(\kappa) \\ 0 & 0 & 0 & 0 \\ \begin{pmatrix} -\kappa^3\, c_2(\kappa) \\ +\kappa^4\, \mu_1\, c_1(\kappa) \end{pmatrix} & \begin{pmatrix} \kappa^3\, c_1(\kappa) \\ +\kappa^4\, \mu_1\, c_2(\kappa) \end{pmatrix} & \begin{pmatrix} \kappa^3\, c_4(\kappa) \\ +\kappa^4\, \mu_1\, c_3(\kappa) \end{pmatrix} & \begin{pmatrix} \kappa^3\, c_3(\kappa) \\ +\kappa^4\, \mu_1\, c_4(\kappa) \end{pmatrix} \\ 0 & 0 & 0 & 0 \end{pmatrix}$$

$$\begin{pmatrix} 0 & 0 & 0 & 0 \\ 0 & 0 & 0 & 0 \\ 0 & -1 & 0 & -1 \\ -\kappa & 0 & -\kappa & 0 \\ 0 & \kappa^2 & 0 & -\kappa^2 \\ -\kappa^2\, c_5(\kappa) & -\kappa^2\, c_6(\kappa) & \kappa^2\, c_7(\kappa) & \kappa^2\, c_8(\kappa) \\ \kappa^3 & 0 & -\kappa^3 & 0 \\ \begin{pmatrix} -\kappa^3\, c_6(\kappa) \\ +\kappa^4\, \mu_2\, c_5(\kappa) \end{pmatrix} & \begin{pmatrix} \kappa^3\, c_5(\kappa) \\ +\kappa^4\, \mu_2\, c_6(\kappa) \end{pmatrix} & \begin{pmatrix} \kappa^3\, c_8(\kappa) \\ +\kappa^4\, \mu_2\, c_7(\kappa) \end{pmatrix} & \begin{pmatrix} \kappa^3\, c_7(\kappa) \\ +\kappa^4\, \mu_2\, c_8(\kappa) \end{pmatrix} \end{pmatrix} \tag{14}$$

with, for the sake of printability, the κ dependent functions $c_1(\kappa) = \sin(x_1\kappa)$, $c_2(\kappa) = \cos(x_1\kappa)$, $c_3(\kappa) = \sinh(x_1\kappa)$, $c_4(\kappa) = \cosh(x_1\kappa)$, $c_5(\kappa) = \sin((x_2 - x_1)\kappa)$, $c_6(\kappa) = \cos((x_2 - x_1)\kappa)$, $c_7(\kappa) = \sinh((x_2 - x_1)\kappa)$, and $c_8(\kappa) = \cosh((x_2 - x_1)\kappa)$, and the constants $\mu_1 = M_1/m$ and $\mu_2 = M_2/m$.

In general, Eq. (14) has only the trivial solution $a_i = 0$ for all $i = 1, \ldots, 8$, which expresses that the system cannot oscillate at all frequencies κ. The eigenmodes can be found by numerically searching for the parameters κ that satisfy $\det(\mathbf{M}(\kappa)) = 0$. The resulting κ_n yield with Eq. (8) the discrete spectrum of eigenfrequencies ω_n. If desired, the system of eight linear equations expressed by Eq. (14) can be solved, too, in order to obtain the shape functions $y_n(x)$ for a specific mode n, by arbitrarily choosing one coefficient, e.g. $a_{n1} = 1$.

Funding
This work was financially supported by the German Aerospace Center (DLR), Project No. 50 RS 1301.

Availability of data and materials
Not applicable.

Authors' contributions
All authors read and approved the final manuscript.

Competing interests
The authors declare that they have no competing interests.

Publisher's Note

Received: 17 November 2017 Accepted: 27 February 2018
Published online: 21 March 2018

References

1. Brown DL, Walker MLR, Szabo J, Huang W, Foster J (2017) Recommended Practice for Use of Faraday Probes in Electric Propulsion Testing. J Propul Power 33:582–613
2. Zhang Z, Tang H, Zhang Z, Wang J, Cao S (2016) A retarding potential analyzer design for keV-level ion thruster beams. Rev Sci Instr 87:123510
3. Celik M, Batishchev O, Martínez-Sánchez M (2010) Use of emission spectroscopy for real-time assessment of relative wall erosion rate of BHT-200 hall thruster for various regimes of operation. Vacuum 84:1085–1091

4. Matsui M, Yokota S, Takayanagi H, Koizumi H, Komurasaki K, Arakawa Y (2006) Plume Characterization of Plasma Thrusters Using Diode-Laser Absorption Spectroscopy. In: 44th AIAA Aerospace Sciences Meeting and Exhibit, Reno, Nevada. American Institute of Aeronautics and Astronautics, Reston. AIAA-2006-767
5. Spektor R, Diamant KD, Beiting EJ, Raitses Y, Fisch NJ (2010) Laser induced fluorescence measurements of the cylindrical Hall thruster plume. Phys Plasmas 17:093502
6. Spethmann A, Trottenberg T, Kersten H (2015) Instrument for spatially resolved simultaneous measurements of forces and currents in particle beams. Rev Sci Instr 86:015107
7. López Ortega A, Katz I, Mikellides IG, Goebel DM (2015) Self-Consistent Model of a High-Power Hall Thruster Plume. IEEE TransPlasma Sci 43:2875–2886
8. Phelps AV (1994) The application of scattering cross sections to ion flux models in discharge sheaths. J Appl Phys 76:747
9. Trottenberg T, Spethmann A, Schneider V, Stahl M, Giesenhagen M, Kersten H (2012) Non-Electrostatic Diagnostics for Ion Beams. Contrib Plasma Phys 52:584–592
10. Rutscher J, Trottenberg T, Kersten H (2013) An instrument for direct measurements of sputtering related momentum transfer to targets. Nucl Instr Meth B 301:47–52
11. Spethmann A, Trottenberg T, Kersten H (2016) Measurement and simulation of the momentum transferred to a surface by deposition of sputtered atoms. Eur Phys J D. 70:255
12. Spethmann A, Trottenberg T, Kersten H (2017) Measurement and simulation of forces generated when a surface is sputtered. Phys Plasmas 24:093501
13. Trottenberg T, Richter T, Kersten H (2015) Measurement of the force exerted on the surface of an object immersed in a plasma. Eur Phys J D. 69:91
14. Czarnetzki U, Tsankov TV (2015) Comment on: Measurement of the force exerted on the surface of an object immersed in a plasma. Eur Phys J D. 69:236
15. Trottenberg T, Kersten H (2017) Measurement of forces exerted by low-temperature plasmas on a plane surface. Plasma Sources Sci Technol 26:055011
16. Spethmann A, Trottenberg T, Kersten H (2013) Spatially Resolved Momentum Flux Measurements for Thruster Plume Diagnostics. In: 33rd International Electric Propulsion Conference, Washington, D.C. Electric Rocket Propulsion Society, Fairview Park. IEPC-2013-079
17. Trottenberg T, Spethmann A, Rutscher J, Kersten H (2012) Non-electrostatic diagnostics for ion beams and sputter effects. Plasma Phys Control Fusion 54:124005
18. Trottenberg T, Rutscher J, Kersten H (2013) Experimental Investigation of Momentum Transfer to Solid Surfaces by the Impact of Energetic Ions and Atoms. In: 33rd International Electric Propulsion Conference, Washington, D.C. Electric Rocket Propulsion Society, Fairview Park. IEPC-2013-329
19. Boisen A, Dohn S, Keller SS, Schmid S, Tenje M (2011) Cantilever-like micromechanical sensors. Rep Prog Phys 74:036101
20. Thurner K, Braun PF, Karrai K (2013) Fabry-Pérot interferometry for long range displacement sensing. Rev Sci Instr 84:095005
21. Thurner K, Braun PF (2013) Absolute distance sensing by two laser optical interferometry. Rev Sci Instr 84:115002, Karrai, K
22. Minoni U, Rovati L, Docchio F (1998) Absolute distance meter based on a frequency-modulated laser diode. Rev Sci Instr. 69:3992–3995
23. Minoni U, Sardini E, Gelmini E, Docchio F, Marioli D (1991) A high-frequency sinusoidal phase-modulation interferometer using an electro-optic modulator: Development and evaluation. Rev Sci Instr. 62:2579–2583
24. Wachtman JB, Lam DG (1959) Young's Modulus of Various Refractory Materials as a Function of Temperature. J Am Ceramic Soc. 42:254–260
25. Landau LD, Lifshitz EM (1986) Theory of Elasticity – 3rd Ed. (Course of Theoretical Physics, Vol. 7). Elsevier, Amsterdam
26. Zeuner M, Scholze F, Neumann H, Chassé T, Otto G, Roth D, Hellmich A, Ocker B (2001) A unique ECR broad beam source for thin film processing. Surf Coat Technol 142–144:11–20